Geophysical Journal International

Geophys. J. Int. (2010) **181,** 1275–1291 doi: 10.1111/j.1365-246X.2010.04601.x

The 2006 March 25 Fin earthquakes (Iran)—insights into the vertical extents of faulting in the Zagros Simply Folded Belt

M. Roustaei,[1,2] E. Nissen,[3] M. Abbassi,[1] A. Gholamzadeh,[1*] M. Ghorashi,[2] M. Tatar,[1] F. Yamini-Fard,[1] E. Bergman,[4] J. Jackson[3] and B. Parsons[5]

[1] *International Institute of Earthquake Engineering and Seismology,* PO Box 19395-3913, *Tehran, Iran*
[2] *Geological Survey of Iran,* PO Box 13185-1494, *Tehran, Iran*
[3] *COMET, Bullard Laboratories, Department of Earth Sciences, University of Cambridge, Madingley Road, Cambridge* CB3 0EZ, *UK.*
E-mail ekn20@cam.ac.uk
[4] *Department of Physics, University of Colorado, Boulder,* CO 80309-0390, *USA*
[5] *COMET, Department of Earth Sciences, University of Oxford, Parks Road, Oxford* OX1 3PR, *UK*

Accepted 2010 March 14. Received 2010 February 11; in original form 2009 July 20

SUMMARY

We investigate the depth of faulting and its connection with surface folding in the Zagros Simply Folded Belt of Iran. Our focus is a sequence of earthquakes (M_w 5.7, 5.5, 5.2, 5.0, 4.9) that struck the Fin region, in the south-eastern Simply Folded Belt, on 2006 March 25. Modelling ground displacements measured with radar interferometry, we find that either N- or S-dipping model reverse faults can reproduce the observed fringe patterns. Despite the uncertainty in fault orientation, we can constrain the vertical extents of rupture to between a top depth of ∼5–6 km and a bottom depth of ∼9–10 km, consistent with the ∼8 km centroid depth of the largest earthquake. We suggest that the faulting ruptured the thick 'Competent Group' of Paleozoic and Mesozoic conglomerates and platform carbonates, which makes up the lower part of the sedimentary cover. The rupture probably terminated within the Precambrian Hormuz salt at its base, and the Cretaceous Gurpi marls at its top. These mechanically weak layers act as barriers to rupture, separating faulting within the Competent Group from deformation in the layers above and below. The pattern of coseismic surface uplift is centred on the common limb of the Fin syncline and Guniz anticline, but is oblique (by 20°) to the trend of these open, symmetric, 'whaleback' folds, and also overlaps a section of the Fin syncline axis. These observations suggest that locally, surface folding is decoupled from the underlying reverse faulting. Although the Fin syncline and Guniz anticline are symmetric structures, some other nearby folds show a strong asymmetry, with steep or overturned southern limbs, consistent with growth above N-dipping reverse faults. This suggests that the Simply Folded Belt contains a combination of forced folds and detachment folds. We also investigate the distribution of locally recorded aftershocks in the weeks following the main earthquakes. Most of these occurred at depths of ∼10–30 km, with a particularly high concentration of events at ∼20–25 km. These aftershocks therefore lie within the crystalline basement rather than the sedimentary cover, and are vertically separated from the main rupture. This study confirms earlier suggestions that earthquakes of M_w 5–6 are capable of being generated within the thick 'Competent Group' of Paleozoic and Mesozoic sediments, as well as in the basement below the Hormuz Salt Formation.

Key words: Radar interferometry; Earthquake source observations; Seismicity and tectonics; Continental tectonics: compressional.

1 INTRODUCTION

In many regions of intracontinental shortening, anticlines form above concealed reverse or thrust faults as a consequence of diminished slip close to the surface, a process known as 'forced folding' or 'fault-propagation folding' (e.g. Yielding *et al.* 1981; Stein & King 1984; Suppe & Medwedeff 1990; Allmendinger & Shaw 2000). In other such areas, anticlines and synclines are instead produced by simple buckling of the uppermost sediments, which may be decoupled from the underlying deformation by mechanically weak layers that act as barriers to rupture; this mechanism is called 'detachment

*Now at: University of Hormozgan, Bandar Abbas, Iran.

folding' (e.g. Davis & Engelder 1985; Mitra 2003). In some cases the weak layers form a décollement (literally: 'ungluing') surface, over which the uppermost layers may slide for large distances. In cases where thrust faults change dip, or where décollements change to a shallower stratigraphic level, folds can also be produced at the surface. This third mechanism of fold generation is termed 'fault-bend folding' (e.g. Suppe & Namson 1979; Suppe 1983).

If we are to understand how fold-and-thrust belts evolve over time, and also accurately assess the seismic hazard in those areas where they are active today, we must first determine the mechanism responsible for the folding visible at the surface. To do this, the geometry of faulting at depth must be known. However, in places where shortening is accommodated within a thick sedimentary cover, faulting may be buried to depths of several kilometres and—in the absence of high-quality information from seismic reflection surveys—the connection with the surface geology can be difficult to establish. Nevertheless, the potential exists to use our modern ability to accurately determine earthquake fault parameters to investigate this problem.

This aim of this study is to establish the geometry of earthquake faulting in some recent earthquakes in the Zagros mountains of Iran, and to investigate the connection between this faulting and surface folding. The Zagros is one of the most seismically active fold-and-thrust belts in the world, and also contains a spectacular surface geology comprising parallel trains of 'whaleback' anticlinal mountains and synclinal valleys. A better understanding of folding and faulting here, where these processes are ongoing, may help inform us about fold-and-thrust belts globally, including those that are no longer active. However, the extent to which various décollements within the thick sedimentary cover have detached the Zagros folds from underlying faulting has been debated for several decades (e.g. O'Brien 1957; Stöcklin, 1968; Falcon 1969; Colman-Sadd 1978), without satisfactory conclusion.

Previous studies of the Zagros have constrained the location of buried faulting either using earthquake seismology or by constructing balanced cross-sections through the range. However, there are significant uncertainties involved in both these methodologies. For Iranian earthquakes studied using teleseismically recorded body-waves, errors in epicentres and depths are ∼10–15 km and ∼4 km, respectively (Engdahl *et al.* 2006). In the Zagros, this makes it difficult to place an earthquake unequivocally beneath one surface fold as opposed to a neighbouring one, and can also cause uncertainty in whether the sedimentary cover or underlying basement was ruptured. Equally, balanced cross-sections through the range are often non-unique, sometimes resulting in profoundly different interpretations of the structure at depth (e.g. McQuarrie 2004; Mouthereau *et al.* 2007). Furthermore, there are very few published seismic reflection profiles with which these transects can be constrained (Sherkati *et al.* 2005; Jahani *et al.* 2009).

We follow an alternative approach to the problem. Using Synthetic Aperture Radar interferometry (InSAR), we map the surface displacements caused by a recent cluster of earthquakes at Fin, in the south-eastern Zagros. By modelling the displacements using elastic dislocation theory, we determine the position, orientation and vertical extents of the causative faulting, and check these results for consistency with teleseismic waveform analysis. These fault plane parameters are then used to discriminate between different models of Zagros deformation. We are also able to compare the earthquake faulting with the distribution of smaller aftershocks, recorded by a local network of seismometers deployed in the region after the main cluster of earthquakes. Finally, we discuss implications for the way in which strain is distributed with depth in the Zagros.

2 GEOLOGICAL AND TECTONIC SETTING

2.1 Overview

Extending for ∼1800 km between northern Iraq and the Strait of Hormuz (inset, Fig. 1), the Zagros mountains comprise the deformed part of the Arabian plate following its continental collision with central Iran, which started in either the Miocene (McQuarrie *et al.* 2003), Oligocene (Agard *et al.* 2005) or Eocene (Allen & Armstrong 2008) and continues to the present day. GPS measurements show that the Zagros currently accommodates almost half of the N–S shortening between Arabia and Eurasia, which is 25 mm yr^{-1} at 56°E (Vernant *et al.* 2004).

The Zagros mountains can be divided into two distinct zones, based on topography, geomorphology, exposed stratigraphy and seismicity. The north-eastern (and topographically highest) part of the range is known as the High Zagros, and the south-western (and topographically lower) part is known as the Simply Folded Belt (SFB) or Simple Folded Zone (Fig. 1).

The High Zagros contains highly imbricated slices of Paleozoic and Mesozoic sediments, as well as fragments of Cretaceous ophiolites (Berberian 1995). In some areas (such as NE of Shiraz), Mesozoic strata are exposed in open folds, with geometries similar to those in the SFB, but in the most part the High Zagros is morphologically very distinct from lower parts of the range. The High Zagros is bounded on its north-eastern side by the Main Zagros Reverse Fault (MZRF), and on its south-western side by the High Zagros Fault (HZF). The MZRF is usually interpreted as the suture between former rocks of the Arabian continental margin and igneous and metamorphic rocks of central Iran (e.g. Stöcklin, 1968), although an alternative view has this contact further to the northeast (e.g. Alavi 1994). The MZRF is no longer active in a reverse sense, although in the northern Zagros part of the same fault zone accommodates a right-lateral component of Arabia–Iran convergence (e.g. Talebian & Jackson 2002; Peyret *et al.* 2008). The HZF is a major, NE-dipping thrust, and in most places marks the southern limit of Paleozoic rocks in the Zagros (Berberian 1995).

The Simply Folded Belt extends from the HZF to the Persian Gulf. Most of the active deformation in the Zagros is concentrated here, presumably having migrated south-westwards from the High Zagros at some earlier stage (e.g. Hessami *et al.* 2001b; Talebian & Jackson 2004; Walpersdorf *et al.* 2006; Oveisi *et al.* 2009). The SFB is itself laterally subdivided into four regions of variable length, width and morphology. From NW to SE, these are the Kirkuk Embayment, the Lurestan Arc, the Dezful Embayment and the Fars Arc (inset, Fig. 1). At the eastern syntaxis of the Fars Arc, also known as the 'Oman Line' (Fig. 1), faulting and folding bend sharply southwards to link up with structures in the Makran accretionary wedge (e.g. Molinaro *et al.* 2004; Regard *et al.* 2004; Bayer *et al.* 2006; Yamini-Fard *et al.* 2007).

Our study area is located within the Fars Arc, which is the largest of the four parts of the SFB, comprising about half of the length of the range and up to ∼250 km in width (Fig. 1). It is this part of the range which we now focus on.

2.2 Geology of the Simply Folded Belt

The SFB contains a thick cover of Arabian passive margin sediments spanning the entire Phanerozoic, which has long been known to exert a strong influence on the style of deformation (e.g. O'Brien 1957; Stöcklin, 1968; Falcon 1969; Colman-Sadd 1978). At the

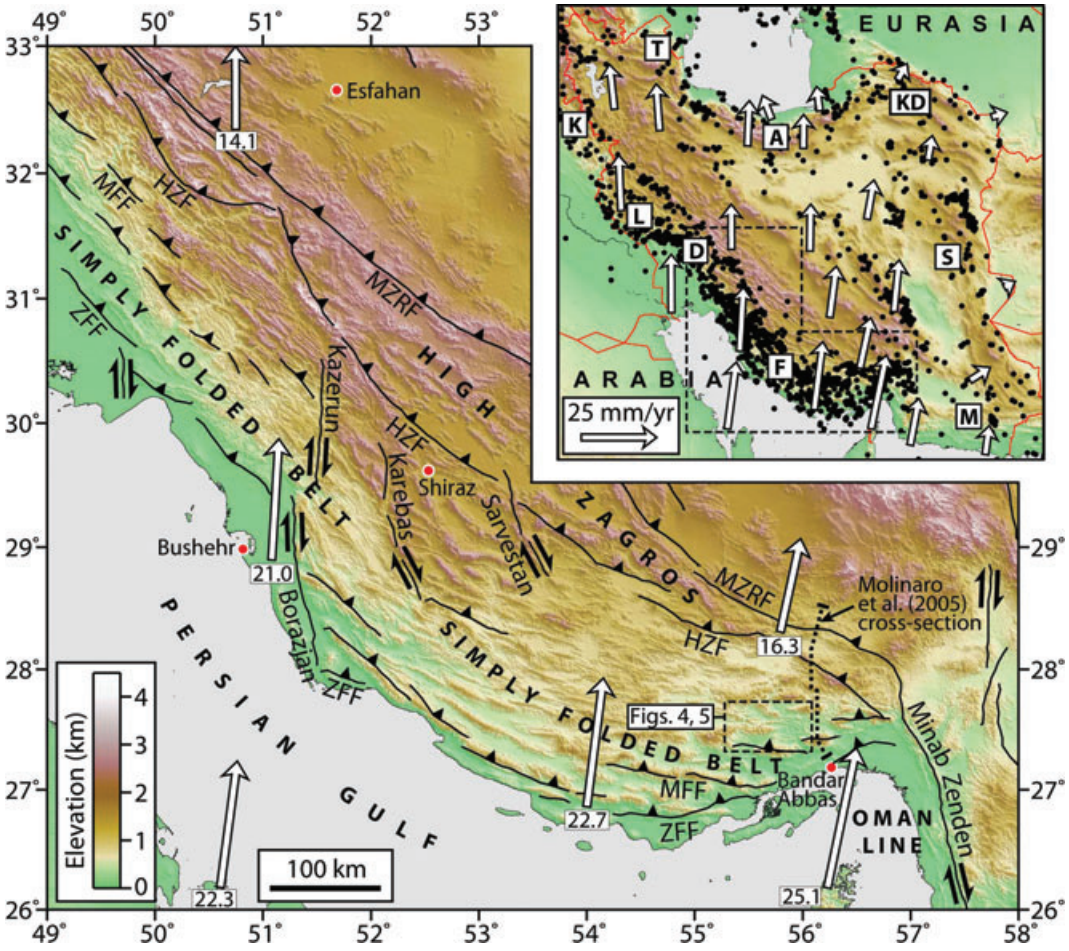

Figure 1. Inset: Topographic map of Iran, showing earthquakes (black dots, from an updated version of the Engdahl *et al.* 1998, catalogue) and GPS velocities relative to stable Eurasia (white arrows, from Vernant *et al.* 2004). Major sections of the Zagros Simply Folded Belt are marked K (Kirkuk Embayment), L (Lurestan Arc), D (Dezful Embayment) and F (Fars Arc). Other major earthquake belts are marked T (Talesh), A (Alborz), KD (Kopeh Dag), S (Sistan) and M (Makran). The location of the main figure is outlined by a dashed black line. Main figure: map of the south-eastern Zagros—comprising the Fars Arc and adjacent parts of the High Zagros—showing topography (illuminated from the NE), GPS velocities (as earlier, with rates in mm yr^{-1}) and major faults. The suture between rocks of the Arabian margin and those of central Iran is marked MZRF (Main Zagros Reverse Fault), and the 'master blind thrusts' of Berberian (1995) are marked HZF (High Zagros Fault), MFF (Mountain Front Fault) and ZFF (Zagros Foredeep Fault). The dotted line north of Bandar Abbas shows the location of the structural cross-section of Molinaro *et al.* (2005), used to estimate the stratigraphic thicknesses in Fig. 2.

base of this sequence lies the late Proterozoic to Cambrian Hormuz Formation, an important layer of mobile salt which outcrops in scattered salt plugs and diapirs within the Fars Arc (Kent 1979). It is not clear what thickness of Hormuz salt remains at depth, nor its lateral extent, although some researchers have suggested that the distinctive morphology of the Dezful Embayment (inset, Fig. 1) owes itself to an absence of Hormuz salt in these areas (e.g. Bahroudi & Koyi 2003).

The Phanerozoic strata comprise competent limestones, dolomites, sandstones and conglomerates, separated by weaker layers of marl and evaporite. Although there are important lateral variations, many of the formations are present along the entire length of the range (e.g. Alavi 2004). The stratigraphy for the far south-eastern Zagros, ∼50 km east of our own study area, is shown in Fig. 2 (Molinaro *et al.* 2005). Here, Paleozoic and lower Mesozoic rocks comprise conglomerates and massive limestones and dolomites, collectively termed the 'Competent Group'; thicknesses of these units are derived from exposures in the High Zagros and are poorly constrained within the SFB itself. Upper Cretaceous to middle Miocene strata encompass a more mixed sequence of mechanically weak marls (Gurpi, Razak and Mishan Formations) interspersed with competent limestones (Asmari and Guri formations); in our study area, the Razak marls are replaced by the Gachsaran evaporites (National Iranian Oil Company 1999). Finally, a switch to coarse, clastic sedimentation in the middle Miocene accompanied the early stages of continental collision.

Estimates of the total stratigraphic thickness range from 10 to 15 km. South of the folded zone in the Persian Gulf, seismic reflection profiles show horizons at 11–15 km depth which are interpreted to be the top of the Hormuz salt (Jahani *et al.* 2009). Onshore, stratigraphic thicknesses are probably slightly smaller, with estimates of ∼12 km in the central SFB (Colman-Sadd 1978) and ∼10 km in the far south-east, close to our study area (Molinaro *et al.* 2005, Fig. 2). Thrusting and folding may have further thickened the cover, but the precise depth to basement is in most places poorly constrained. In the Ghir region (∼28°N, ∼53°E), a basement depth of ∼11 km was inferred by inverting the arrival times of locally recorded earthquakes (Hatzfeld *et al.* 2003).

The surface geology and topography of the SFB are characterized by parallel trains of folds, their 'whaleback' shapes expressed

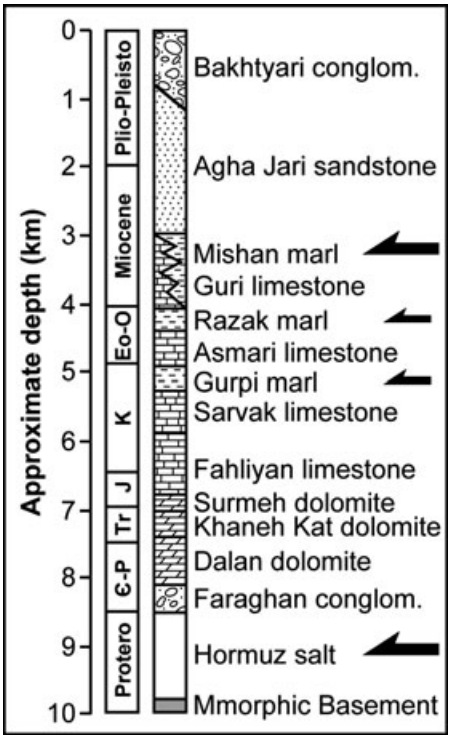

Figure 2. Simplified stratigraphic column for the far south-eastern Zagros, from work by Molinaro *et al.* (2005) based ∼50 km east of our own study area (dotted line, Fig. 1). The depths are poorly constrained and should only be considered approximate. Possible detachment levels are picked out by black arrows; note that in our own study area, the Razak formation is replaced by the Gachsaran formation, consisting of marls and anhydrites (National Iranian Oil Company 1999). The 'Competent Group' comprises the package of relatively competent sediments from the Cambrian Faraghan conglomerate up to the Cretaceous Sarvak limestone.

in resistant units such as the Asmari limestone (e.g. Colman-Sadd 1978). Individual folds are typically ∼10 km in half-wavelength and many tens of kilometres in length. Many of the folds are concentric, although some anticlines do exhibit markedly steepened or even overturned southern limbs. GPS velocities (Walpersdorf *et al.* 2006) and geomorphological observations (Oveisi *et al.* 2009) from the Fars Arc show active shortening to be concentrated within the frontal part of the SFB, close to the Persian Gulf coastline. These results are consistent with stratigraphical evidence supporting a south-westwards propagation of folding within the SFB (Hessami *et al.* 2001b).

Several structural transects of the SFB have been published, with the aim of characterizing the deformation and establishing the total amount of shortening. These include a number of balanced sections through the Fars Arc (Hessami *et al.* 2001b; McQuarrie 2004; Sherkati & Letouzey 2004; Molinaro *et al.* 2005; Sherkati *et al.* 2006; Alavi 2007; Mouthereau *et al.* 2007), and others further north-west (e.g. Blanc *et al.* 2003; Sepehr *et al.* 2006). However, the style of deformation described varies markedly from one study to the next. For instance, in balanced sections through exactly the same part of the central Fars Arc, McQuarrie (2004) depicts a mixture of fault propagation and fault-bend folding produced by faults in the lower sedimentary cover, but Mouthereau *et al.* (2007) portray these same structures as pure detachment folds formed by simple buckling. Equally, McQuarrie (2004) restricts faults to within the sedimentary cover, whereas Mouthereau *et al.* (2007) place them almost exclusively within the underlying basement.

Some of these studies invoke a two-stage model of deformation, which involves both detachment and forced folding, although at different times (Molinaro *et al.* 2005; Sherkati *et al.* 2006). In this model, shortening is at first accommodated by buckling. Later on, migration of mobile Hormuz salt into the cores of anticlines promotes faulting within the lower sedimentary cover, thereby steepening some of the SW-facing fold limbs. These faults propagate upwards either from a detachment in the Hormuz salt or from deeper faults which break through the basement-cover interface. This two-stage model is derived from an apparent overprinting of detachment folding with forced folding in the far south-eastern SFB, ∼50 km east of our own study area (Molinaro *et al.* 2005).

2.3 Seismicity of the Simply Folded Belt

Fig. 3 shows earthquake focal mechanisms and centroid depths in the south-eastern Zagros, updated from Talebian & Jackson (2004) and references therein, Walker *et al.* (2005), Nissen *et al.* (2007), Adams *et al.* (2009) and the Global CMT catalogue. Focal mechanisms are dominated by reverse-faulting, with frequent earthquakes of M_w 5–6 and occasional larger events up to M_w 6.7. These faults follows the local trend of the range, striking ∼NW–SE in north-western Fars (as well as further to the north-west) but changing to ∼E–W in the southeast. A series of N–S strike-slip faults in the central SFB (Fig. 1) are thought to accommodate a component of range-parallel extension (Baker *et al.* 1993; Hessami *et al.* 2001a; Talebian & Jackson 2004), but are not important for the purposes of this study.

The centroid depths of waveform-modelled earthquakes mostly lie in the range ∼4–19 km (Talebian & Jackson 2004; Adams *et al.* 2009, Fig. 3). Two deeper earthquakes (∼28 km), located just north of the eastern syntaxis of the Zagros (inset, Fig. 3), may represent underthrusting of the Arabian shield along the Oman Line (Talebian & Jackson 2004). However, in the Zagros fold-and-thrust belt itself there is no evidence for earthquakes occurring along a low angle detachment, as is observed, for example, beneath the Himalaya (e.g. Ni & Barazangi 1986). On the contrary, many reverse faulting earthquakes in the SFB have relatively steep dips (30–60°), possibly inherited from normal faults that formed during stretching of the Arabian margin in the Mesozoic and early Tertiary (Jackson 1980).

Earthquakes in the depth range ∼12–19 km are probably located within the crystalline basement, and are sometimes concentrated within discrete linear bands or zones, each corresponding to a significant change in elevation and stratigraphical level at the surface. Based on this observation, Berberian (1995) proposed that shortening within the basement is accommodated on a small number of N- or NE-dipping 'master blind thrusts', which are plotted in Fig. 1. Although these faults do not break the surface, sediments in their hanging walls are typically folded into steeply asymmetric, S- or SW-verging anticlines. This suggests that the major basement faults continue upwards into the sedimentary cover, where they control the local folding.

The shallowest earthquakes, with centroid depths in the range ∼4–8 km, are almost certainly located within the sedimentary cover (Lohman & Simons 2005; Nissen *et al.* 2007; Adams *et al.* 2009). These events are not known to rupture the surface, probably because mechanically weak marls and evaporites act as barriers to rupture (e.g. Berberian 1995; Talebian & Jackson 2004). One thrust earthquake that did break the surface was the 1990

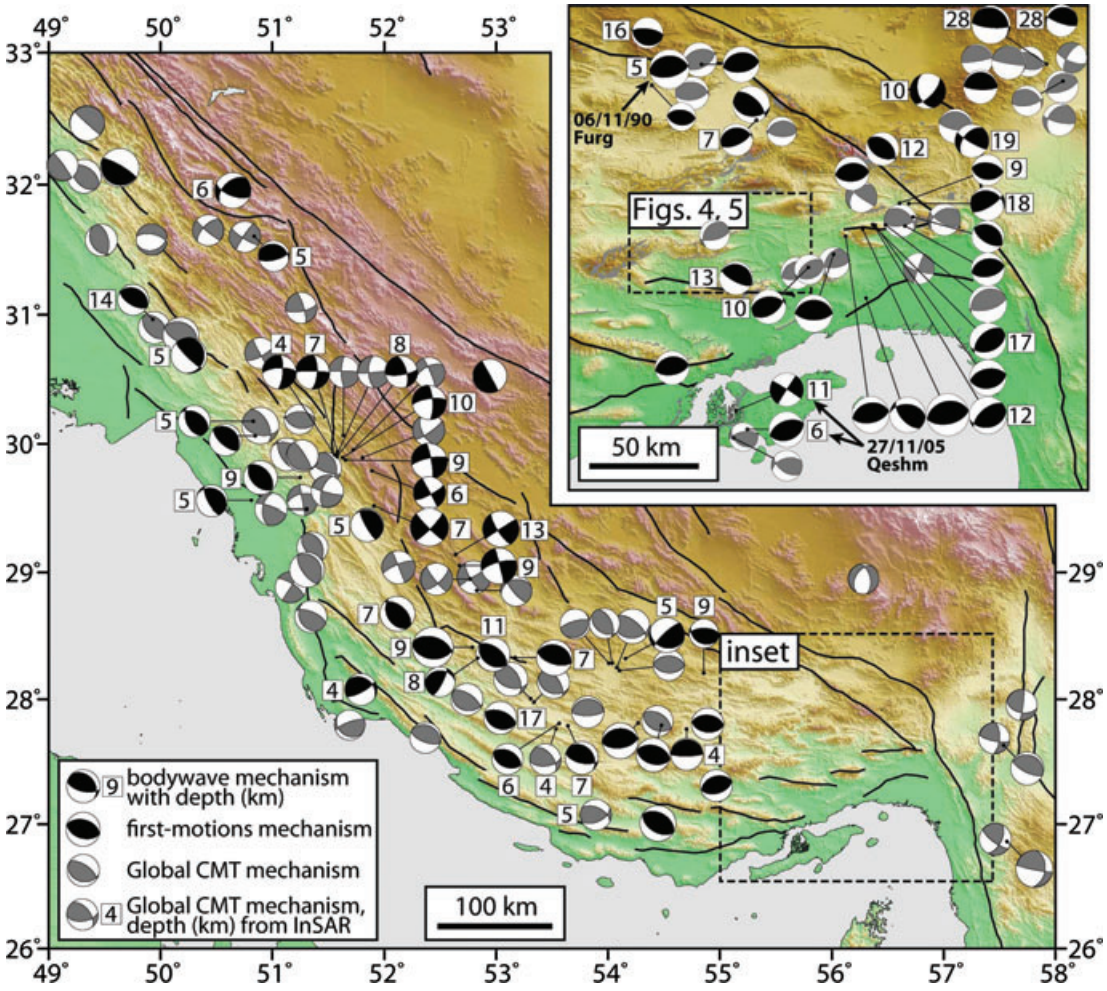

Figure 3. Earthquake focal mechanisms in the south-eastern Zagros. Black mechanisms span the period 1964–2005 and are from waveform modelling (with centroid depths in km) or first-motions (without centroid depths); these are from Talebian & Jackson (2002) and references therein, Walker *et al.* (2005), Nissen *et al.* (2007) and Adams *et al.* (2009). Grey mechanisms are from the Global CMT catalogue and span the period 1976–2005; two of these have well-constrained depths from InSAR modelling (Lohman & Simons 2005). All earthquakes are plotted at locations from the Engdahl *et al.* (2006) catalogue and its subsequent updates.

November 6 Furg earthquake (M_w 6.4, centroid depth 5 km), which produced ∼15 km of surface ruptures in the far eastern Zagros (Walker *et al.* 2005, inset, Fig. 3). However, this event probably involved a reactivation of part of the High Zagros Fault, and is considered unrepresentative of earthquake faulting in the SFB.

For a great many earthquakes in the SFB, centroid depths are within an intermediate range of ∼8–12 km. Given the ∼4 km errors in these depths (Engdahl *et al.* 2006), as well as uncertainties in the thickness of the sedimentary cover, it is not clear whether these earthquakes ruptured the cover or the underlying basement (or both). However, measuring the surface displacements in such earthquakes using InSAR offers a way of establishing their depths with a greater degree of precision. Because the wavelength of a coseismic surface signal depends on the depth at which slip occurs, these displacements can be modelled using elastic dislocation theory (Okada 1985) to determine the earthquake source parameters, including the top and bottom depths of the ruptured fault plane (e.g. Wright *et al.* 1999).

2.4 Previous InSAR work in the Simply Folded Belt

Since InSAR was developed in the early 1990's there have been unusually few earthquakes in the SFB compared to previous decades; there is also a relative scarcity of SAR data available for the region (Lohman & Simons 2005). As a result, few earthquakes in the SFB have been studied with InSAR. Lohman & Simons (2005) located four earthquakes in the region, but these are relatively small events (M_w 4.7–5.4) and in each case displacements were measured in a single viewing geometry, preventing a full assessment of the source parameters.

Nissen *et al.* (2007) studied the larger (M_w 6.0), 2005 Qeshm Island earthquake (labelled on the inset, Fig. 3a). In this study, data from both ascending (moving north) and descending (moving south) satellite orbit tracks were used, providing an additional component of the displacement vector. Elastic dislocation models of this earthquake placed fault slip at depths of ∼4 to ∼8 km, probably mostly within the sedimentary cover. Although coseismic uplift was centred on an anticline, the complicated surface structure of Qeshm Island

(consisting of orthogonal sets of fold axes) obscured the connection between faulting at depth and folding at the surface.

3 THE 2006 MARCH 25 FIN EARTHQUAKES

On 2006 March 25 at 07:29 UTC (10:59 local time), a M_w 5.7 earthquake struck the Fin region in the south-eastern Simply Folded Belt (Fig. 4a). This earthquake was followed by aftershocks at 09:55 (M_w 5.5), 10:00 (M_w 5.2), 11:02 (M_w 5.0) and 12:13 UTC (M_w 4.9). There were no reports of injuries or loss of life, but buildings in the village of Bonab suffered minor damage and the earthquakes triggered land sliding in the area between Bonab and Fin. There were no indications of any surface ruptures.

The surface geology of the Fin region comprises a series of parallel, E–W trending folds that expose sediments ranging from the Pliocene–Pleistocene Bakhtyari conglomerates down to the Eocene–Oligocene Asmari limestone (Fig. 4b). Proterozoic–Cambrian Hormuz salt is also observed in a number of salt plugs, but otherwise strata older than the Eocene are almost entirely absent at the surface in the area shown in Fig. 4. The folds themselves are a mixture of concentric, open structures (e.g. Fin syncline, Guniz and Handun anticlines) and anticlines that verge strongly toward the south, with steepened or even overturned southern limbs (e.g. Anguru and Ginau anticlines). Some of the anticlines also have exposures of Hormuz salt in their cores (e.g. Guniz, Handun and Tashkend). Nevertheless, there are no complications from orthogonal structures, as was the case at Qeshm Island (Nissen *et al.* 2007). The 2006 Fin earthquakes therefore provide an ideal opportunity to study the connection between faulting and folding in the SFB.

3.1 Seismology

Focal mechanisms for all five earthquakes are available from the Global CMT catalogue. These indicate almost pure reverse slip on E–W striking fault planes, which dip either ∼30°N or ∼60°S.

To obtain improved source parameters and centroid depths for the largest two earthquakes (07:29 and 09:55 UTC), we modelled teleseismically recorded P and SH bodywaves. Seismograms were inverted using the MT5 version (Zwick *et al.* 1994) of McCaffrey & Abers's (1988) algorithm. Assuming a double-couple, point source embedded in a half-space with V_p = 5.7 m s^{-1}, V_s = 3.3 m s^{-1} and $\rho = 2.6 \times 10^3$ kg m^{-3} (these values are consistent with the upper part of the velocity structure calculated from locally recorded aftershock arrival times in Section 4), we solved for the minimum-misfit strike, dip, rake, centroid depth, seismic moment and source time function for each earthquake. This approach is now routine for studies of this type, and does not warrant an additional description here (for a full summary, see Molnar & Lyon-Caen 1989).

Source parameters for our minimum-misfit bodywave models are listed in Table 1, and the focal mechanisms, together with observed and synthetic seismograms, are shown in Appendix A, Figs A1 and A2. Our models have similar strikes, dips and rakes to the Global CMT mechanisms, with almost pure reverse motion on N- or S-dipping nodal planes. Seismic moments are somewhat lower than those listed in the Global CMT catalogue, which are 7.8 × 10^{17} Nm for the 07:29 earthquake, and 2.1 × 10^{17} Nm for the 09:55 earthquake. The 'double pulse' shapes of both source time functions represent artefacts of the modelling and should not be considered significant. On the other hand, the overall durations of these source time functions are well resolved, at 6 and 4 s, respectively; these values are consistent with the overall length of faulting obtained from modelling ground displacements (Section 3.2), assuming a realistic rupture velocity of 2–3 km s^{-1}. Finally, the centroid depths

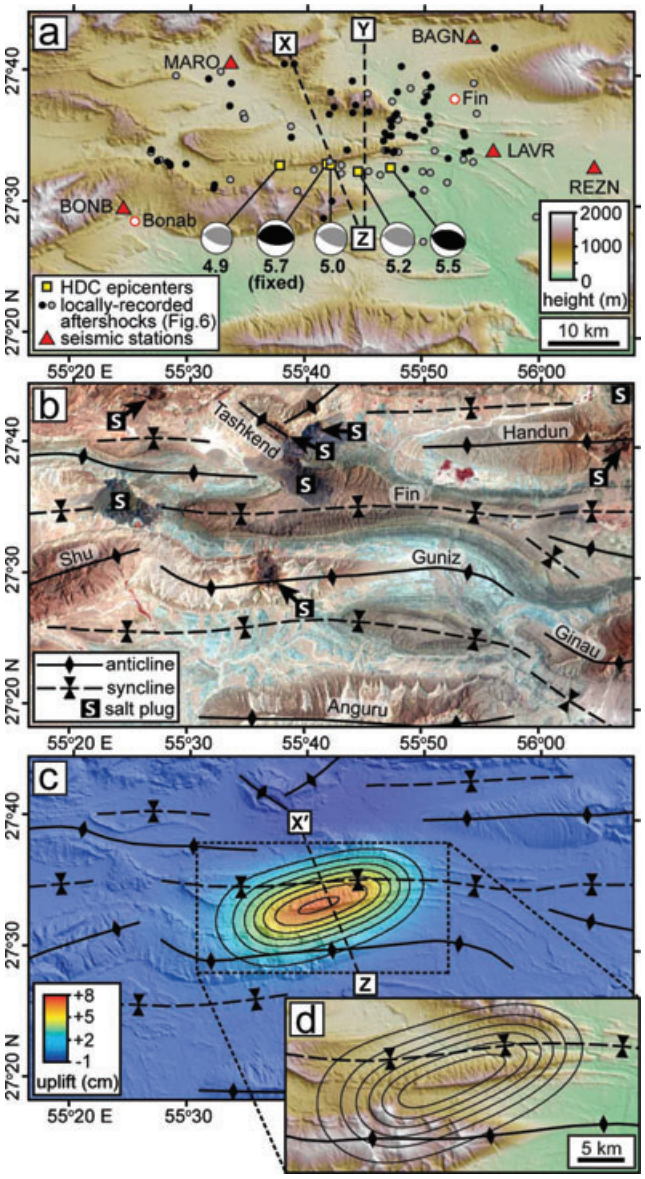

Figure 4. (a) Focal mechanisms of the 2006 March 25 earthquakes, locally recorded aftershocks, and artificially illuminated Shuttle Radar Topography Mission (SRTM) digital topography. Black mechanisms are bodywave models and grey mechanisms are from the Global CMT catalogue, and moment magnitudes are plotted next to each focal sphere. Yellow squares are epicentres relative to the 07:29 mainshock (M_w 5.7), calculated by hypocentroidal decomposition. Black dots are the best-recorded, 55 locally recorded aftershocks (each with horizontal and vertical errors ≤3 km), and grey dots are a further 32 locally recorded events (with errors ≤5 km). *X*–*Z* and *Y*–*Z* show lines of cross-section through these aftershocks, which are plotted in Figs 6(b) and (c). (b) Landsat image (RGB 421) annotated with major fold axes and exposed Hormuz salt plugs; vegetation appears red. (c) Surface uplift predicted by our N-dipping, single-fault interferometric model (A), with contours at 1 cm intervals. *X*′–*Z* is the line of cross-section through the model uplift and the geology, plotted in Figs 7(a) and (b). (d) The same surface uplift contours plotted on topography.

Table 1. Fault plane parameters for the 25 March 2006 07:29 and 09:55 UTC earthquakes, from modelling P and SH bodywaves and line-of-sight displacements.

	07:29[a]	09:55[a]	InSAR Model A	InSAR Model B	InSAR Model C (two faults)[b]		InSAR Model D (two faults)[b]	
Strike	271°	279°	251° ± 3	75° ± 3	271°	279°	93°	107°
Dip	30°N	45°N	34° ± 7N	45° ± 5S	30°N	45°N	60°S	45° S
Rake	88°	84°	75° ± 12	92° ± 10	88°	84°	91°	95°
Slip (m)	–	–	0.36 ± 0.17	0.39 ± 0.17	0.35	0.25	0.35	0.25
Eastings (km)	–	–	374.6 ± 1.1	368.8 ± 1.0	366.1 ± 0.7	374.7 ± 0.6	366.8 ± 0.7	377.7 ± 0.6
Northings (km)	–	–	3040.1 ± 2.0	3056.7 ± 0.8	3036.2 ± 1.0	3044.9 ± 0.5	3053.1 ± 0.3	3057.8 ± .7
Length (km)	–	–	20.7 ± 1.4	20.0 ± 1.3	14.5 ± 1.3	11.1 ± 1.4	14.3 ± 1.4	11.7 ± 1.1
Top (km)	–	–	5.8 ± 0.8	6.1 ± 0.9	6.2 ± 0.4	4.6 ± 0.4	5.5 ± 0.4	4.8 ± 0.4
Bottom (km)	–	–	9.0 ± 0.6	10.1 ± 0.8	8.4 ± 0.6	9.5 ± 1.2	9.3 ± 0.9	9.1 ± 1.0
Centroid (km)	8 ± 3	4 ± 2	7.4 ± 0.6	8.1 ± 0.6	7.3 ± 0.5	7.0 ± 0.7	7.4 ± 0.6	7.0 ± 0.7
Moment ($\times 10^{17}$ Nm)	4.7 ± 2.0	1.9 ± 0.5	10.8 ± 1.3	11.1 ± 1.1	6.2 ± 0.9	5.3 ± 0.9	6.2 ± 0.9	5.0 ± 0.8
M_w	5.7	5.5	6.0	6.0	5.8	5.8	5.8	5.7

Note: *Eastings* and *Northings* are the surface projection of the centre of the model fault plane in UTM zone 40 coordinates (km). *Top* and *Bottom* are the top and bottom depths of the model fault plane; *Centroid* refers to the centroid depth for the bodywave models, and the depth of the centre of the fault plane for the InSAR-derived models. Errors in bodywave depths and moments were estimated using the procedure of Molnar and Lyon-Caen (1989). Errors in InSAR-derived models are at the 1σ level.

[a] Alternative nodal plane strikes, dips and rakes are provided in Figs A1 and A2.

[b] Strike, dip, rake and slip of both faults fixed during inversion.

are 8 ± 3 km for the 07:29 earthquake and 4 ± 2 km for the 09:55 event.

We also calculated improved relative locations for the five main earthquakes, using the hypocentroidal decomposition (HDC) method of Jordan & Sverdrup (1981). Again, this procedure is now widely used and is not described in detail here. The first and largest earthquake (07:29) was fixed to lie at the centre of the coseismic InSAR signal (Section 3.2), at a depth of 8 km, and the four smaller earthquakes were relocated relative to this first event. Our results are plotted on Fig. 4a, and have relative accuracies of ∼1 km. Three of the smaller earthquakes (09:55, 10:00 and 11:02) lie roughly east of the main earthquake, whereas the fourth (12:13) is positioned to the west. This pattern is consistent with the rupturing of along-strike sections of an E–W fault zone, although it is not clear whether the five earthquakes involved faults dipping in only one direction (either N or S), or a combination of N- and S-dipping faults.

3.2 Radar interferometry

We constructed four interferograms spanning the 2006 March 25 earthquakes, using measurements from the European Space Agency Envisat satellite (Table 2). Three of these use descending satellite passes, with an ∼ENE-facing pointing vector (between the satellite and the ground) and an incidence angle of 23° along the centre of the interferogram swaths (measured from the vertical). Two of the descending interferograms were constructed from Track 435 data and share the same second ('slave') radar scene; the third was produced using Track 206 data. A fourth interferogram, produced from ascending satellite passes (Track 328) with a ∼WNW-facing pointing vector and a centre-scene incidence angle of 41°, provides an additional component of the displacement vector.

All four interferograms display a clear, coseismic signal centred about 20 km WSW of the town of Fin (Figs 5a–d). In each case, the signal consists of an elliptical, WSW–ENE-trending pattern of displacements. These patterns contain two full fringes, indicating peak displacements of about two radar half-wavelengths (or ∼6 cm) towards the satellites. Although the peak displacements in the ascending-track interferogram are situated ∼3–6 km west of those in the descending ones, the broad overlap of ascending and descending fringe patterns implies that line-of-sight displacements are dominated by vertical uplift, rather than any strike-slip component (e.g. Nissen *et al.* 2007). Some of the interferograms also display apparent displacements away from the satellite in areas just N and S of the ellipse patterns. However, these signals are only about half a fringe in magnitude, similar to the level of atmospheric noise observed in other parts of the interferograms. Because of this, we cannot be certain whether these represent real surface displacements or atmospheric effects.

Table 2. Envisat advanced synthetic aperture radar (ASAR) data used to produce our interferograms.

Pass	Mode	i	Track	Date 1	Orbit 1	Date 2	Orbit 2	Δt (days)	$B_\perp$ (m)	H_a (m)
Desc.	IS2	23°	435	29-Dec-05	20028	18-May-06	22 032	140	41	229
Desc.	IS2	23°	435	09-Mar-06	21030	18-May-06	22 032	70	37	254
Desc.	IS2	23°	206	17-May-05	16793	02-May-06	21 803	350	52	181
Asc.	IS6	41°	328	25-May-05	16915	14-Jun-06	22 426	385	86	109

Note: *Mode* is the Envisat acquisition mode, and *i* is the incidence angle at the centre of the radar swath, measured from the vertical (incidence angles local to the actual earthquake signal are shown in Fig. 5). The first ('master') image of each pair was acquired on *Date 1*, and the second ('slave') on *Date 2*, separated by δt days. The perpendicular baseline between the orbits in each pass is $B_\perp$ m, and the altitude of ambiguity H_am. Interferograms were constructed using GAMMA processing software (Werner *et al.* 2000), and the topographic phase contribution removed was using SRTM topography (Farr & Kobrick 2000).

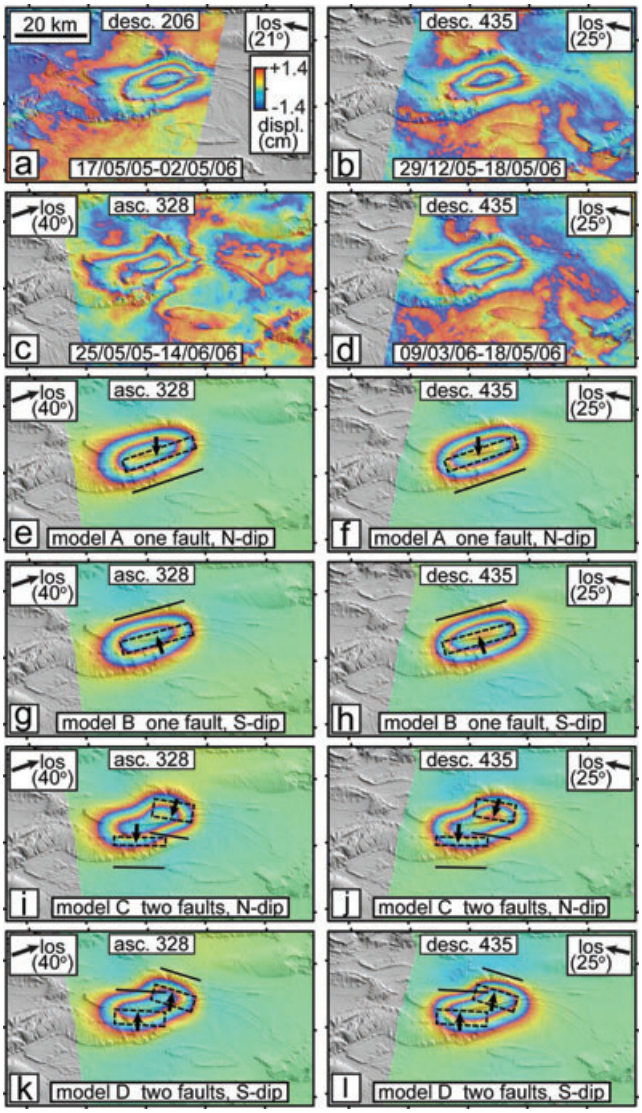

Figure 5. Observed (a–d) and model (e–l) interferograms spanning the 2006 Fin earthquakes, overlain on artificially shaded SRTM topography and with the same map extents as Fig. 4. The satellite line-of-sight (los) and local incidence angle (measured from the vertical) are plotted in white boxes in the corner of each interferogram. (The local incidence angles are different from the centre-scene angles listed in Table 2; this is because the earthquake signal is situated on the western sides of the Track 328 and 435 swaths, and on the eastern side of the Track 206 swath.) Each cycle of colour (or fringe) represents a displacement of one radar wavelength (2.8 cm) in the satellite los. In (e)–(l), dashed black lines outline the model fault planes in map view; solid black lines show their up-dip projection at the surface; and black arrows show the model slip vector (the motion of the hanging wall relative to the footwall). Model A is for a single, N-dipping fault plane, and model B a S-dipping one. For model C we use the N-dipping bodywave nodal planes, and for model D we use the S-dipping nodal planes (Table 1).

There is no sharp discontinuity between displacements toward the satellites from the apparent displacements away from it, indicating that whatever slip occurred at depth did not reach the surface. In cases of buried earthquakes, the surface projection of the fault is indicated by the most closely packed fringes. For the Fin earthquakes, this would place the surface projection of faulting along either the northern or southern edge of the elliptical fringe pattern, although it is not immediately clear which.

To determine fault plane parameters from these displacements, the interferograms were first resampled to reduce each data set to a manageable size. At first we experimented with a quadtree algorithm to concentrate sampling in areas of high deformation gradients (e.g. Jónsson *et al.* 2002), but we found that areas just outside the main ellipse pattern were poorly represented in the resulting data sets. These areas might contain important information about the faulting, so we instead chose to resample the interferograms with a regular grid spacing of datapoints. Finally, we calculated the true, local line-of-sight pointing vector for each datapoint.

Faulting was represented as a single, rectangular dislocation in an elastic half-space (Okada 1985) with Lamé parameters ($\mu = \lambda = 2.8 \times 10^{10}$ Pa) that are consistent with the seismic velocities used in the bodywave modelling. We used a Powell's algorithm (Press *et al.* 1992) with multiple Montecarlo restarts to minimize the square misfit between observed and model line-of-sight displacements (e.g. Wright *et al.* 1999), solving for the strike, dip, rake, amount of slip, latitude, longitude, length, and top and bottom depths of the fault. We also solved for a static shift in the measured displacements (to account for ambiguities in the zero-displacement level), and displacement gradients in the N–S and E–W directions (to account for residual orbital phase ramps). In the inversion, the two descending-track 435 interferograms—which share the same slave scene—were each given half the weighting of descending-track 206 and ascending-track 328 data sets.

Minimum-misfit model parameters are given under 'model A' in Table 1, and model interferograms are shown in Figs 5(e) and (f). The downdip width of the model fault (∼6 km) is small compared with its length (∼21 km). Using earthquake scaling relationships, the fault-plane dimensions of the largest, 07:29 and 09:55 earthquakes are probably ∼7 and ∼5 km, respectively (Appendix B). From the relocated HDC epicentres, we also know that these two events occurred along strike from one another. Our InSAR-derived model is therefore likely to represent the combined displacements of these two earthquakes.

To investigate errors and trade-offs in our fault plane parameters, we modelled 200 synthetic data sets, created by perturbing the original data with noise characteristic of the undeformed parts of the interferograms (e.g. Parsons *et al.* 2006). Some of the resulting fault-plane parameters include unrealistically high values of slip on very narrow fault planes, and we discount those results with more than 1 m slip. Around two thirds of the realistic inversion results have N-dipping fault planes; these were used to calculate the 1σ errors for model A in Table 1. Most of the rest of the realistic inversion results contain S-dipping fault planes, providing an alternative, S-dipping model. This model is labelled 'model B' in Table 1, and model interferograms are shown in Fig. 5(g) and (h).

There are significant, ∼20° discrepancies between the ∼ENE–WSW strike of the InSAR-derived model faults and the ∼E–W strike of the bodywave solutions (as well as the ∼E–W trend of folds at the surface). To investigate this, we modelled the interferometric data again, this time solving for slip on two separate faults whose strikes, dips and rakes are fixed to the values of the bodywave models. We also fixed the slip on the two fault planes to 0.35 and 0.25 m, values which are consistent with the bodywave moments (Table 1). We find that these models can successfully reproduce the observed, WSW–ENE elliptical fringe patterns, by offsetting the two faults in an en echelon fashion (models C and D, Table 1, Figs 5i–l). However, the sense of offset is inconsistent with the relative locations calculated by HDC (Fig. 4a), which place the

09:55 aftershock along strike (due east) of the mainshock, rather than to the northeast. The discrepancy in strike between the single-fault InSAR models and the bodywave models are likely to reflect other fault parameter trade-offs, and cannot be explained by an en echelon pattern of fault segments.

From the arguments earlier, it is clear that we are unable to constrain the orientation of the faulting from the surface displacements alone. However, what we are most interested in is the extents of slip at depth, and the relationship between the vertical uplift and the surface geology.

Errors in the top and bottom depths of InSAR models A and B are less than 1 km at the 1σ level, and reflect a negative trade-off between slip and downdip fault width. The errors for models C and D are 0.4 km for the top depth and 0.6–1.2 km for the bottom depth; the amount of slip is fixed in these inversions (as well as the orientation of the faults), and these errors instead reflect other trade-offs, including one between the top and bottom depths of the fault plane and the latitude of its projected surface trace (a negative trade-off in the case of the N-dipping model C, but a positive one for S-dipping model D).

Considering all four models together, the top depth is 5.4 ± 0.8 km, the bottom depth 9.3 ± 0.9 km and the centre of the faulting 7.5 ± 0.6 km. These figures are consistent with the 8 ± 3 and 4 ± 2 km centroid depths obtained for the 07:29 and 09:55 earthquakes from seismology (Section 3.1).

To further test how tightly constrained these depths are, we increased the size of each model fault plane and then divided it into 2×2 km patches, before solving for distributed slip (Wright *et al.* 2004). In each case, we find that the vertical extents of slip are not significantly changed from the uniform slip models, with negligible slip above ∼5 km and below ∼10 km.

Overall, our InSAR-derived models suggest that faulting primarily ruptured the lower part of the sedimentary cover, probably within the so-called 'Competent Group' of mechanically strong sediments situated between the Hormuz salt and Gurpi marls, both well-known detachment horizons (Fig. 2). However, given the trade-offs in fault parameters and the considerable uncertainties in the thickness of the sedimentary cover, we cannot be certain that the earthquakes did not also rupture into adjacent layers—either above, into the Cenozoic part of the sedimentary cover, or below, into the uppermost crystalline basement.

4 LOCALLY RECORDED AFTERSHOCKS

In addition to our teleseismic and radar measurements of the Fin earthquake sequence, we also determined the distribution of smaller aftershocks using data collected from a local network of portable, three-component seismometers. The stations MARO, REZN, ALVR and BONB (Fig. 4a) were deployed on 2006 April 11, April 12, April 13 and April 19, respectively, and recorded until mid-June 2006. These were complemented by a network of 18 seismometers (including BAGN on Fig. 4a) deployed in early March in the area east of Fin, where a M_w 6.0 earthquake had struck on 2006 February 28 (Gholamzadeh *et al.* 2009). Details of the instruments and data processing techniques we used are provided by Tatar *et al.* (2005).

A total of 383 aftershocks, ranging in magnitude from ∼1 to ∼4, were recorded in the region shown Fig. 4. At first, these were located with a standard half-space model ($V_p = 6.0\,\mathrm{km\,s^{-1}}$) using the HYPO71 program (Lee & Lahr 1972). Next, we selected a subset containing the 87 best-recorded earthquakes, each with an azimuthal gap of $<270^\circ$ and most having both P and S phases recorded at more than one of the closest five stations. The arrival times of these 87 earthquakes were then inverted using the VELEST program (Kissling 1988), which allows a more appropriate, layered velocity structure and improved hypocenters to be calculated simultaneously. Randomly perturbed starting models were used to ensure convergence to the final structure (e.g. Hatzfeld *et al.* 2003). The best-fit velocity structure is shown in Appendix C (Table C1). Because of the small number of readings and the poor azimuthal coverage of the temporary network, this model is unlikely to provide an accurate measure of the thickness of the sedimentary cover, but it does offer a useful constraint on the velocities and elastic properties of the region.

Of the 87 best-recorded aftershocks, 55 have a root mean square residual (the average difference between observed and calculated arrival times) of <0.3 s, an azimuthal gap of $<200^\circ$, and formal horizontal and vertical errors of ≤ 3 km. These aftershocks are listed in Appendix C (Table C2), and plotted as black dots on Fig. 4(a). On the same figure, we also plot the remaining 32 best-recorded aftershocks as grey dots. These events have azimuthal gaps $<270^\circ$ and formal horizontal and vertical errors of ≤ 5 km.

A histogram of aftershock depths is shown in Fig. 6(a). As on Fig. 4(a), the 55 best-recorded earthquakes are represented in black, and the other 32 aftershocks in grey. Almost all of the aftershocks lie in the depth range 10–30 km, and there is a particularly high concentration of well-recorded aftershocks (in black) at 20–25 km. To further test how well-resolved these depths are, we recalculated aftershock hypocenters using a variety of different velocity structures. Depending on the velocity structure used, depths changed by up to 2–3 km. In all cases, however, very few aftershocks were placed shallower than 10 km, and maximum depths were between 25 and 30 km.

The vast majority of aftershocks are therefore significantly deeper than the main earthquake rupture (∼5–10 km) and are probably concentrated within the crystalline basement. In this sense the Fin region resembles that of Ghir (∼28°N, ∼53°E), where microearthquakes are concentrated at well-defined depths of 8–15 km, probably also mostly within the basement (Tatar *et al.* 2004). However, the maximum depths at Fin (∼25–30 km) are significantly deeper than those at Ghir (∼20 km), possibly indicating that the thickness of the seismogenic layer varies along the length of the range.

To investigate the relationship between the main faulting and the aftershocks further, we plot cross-sections through the aftershock hypocenters and our model faults (Figs 6b and c). There are no clear indications that the aftershocks form a downward extension of the main faulting, although this may reflect the uncertainties in hypocenter depths and horizontal locations.

The aftershocks demonstrate that locally, the crust is seismogenic to depths of ∼25–30 km. Clearly, the main Fin earthquakes did not rupture the full thickness of the seismogenic layer. Instead, it is likely that the rupture terminated, or was at least strongly attenuated, within the mechanically weak Hormuz Salt formation at the base of the sedimentary cover. The redistribution of mass caused by faulting in the lower sedimentary cover, which occurred in a matter of seconds, altered the load on the basement and triggered these deep aftershocks.

The vertical separation of a shallow mainshock rupture and deeper aftershocks was also observed for earthquakes at Bam, in eastern Iran (Tatar *et al.* 2005; Jackson *et al.* 2006), and at Tottori, in Japan (Semmane *et al.* 2005). In these cases there are no known, mechanically weak layers at depth and the reasons for the separation remain little understood.

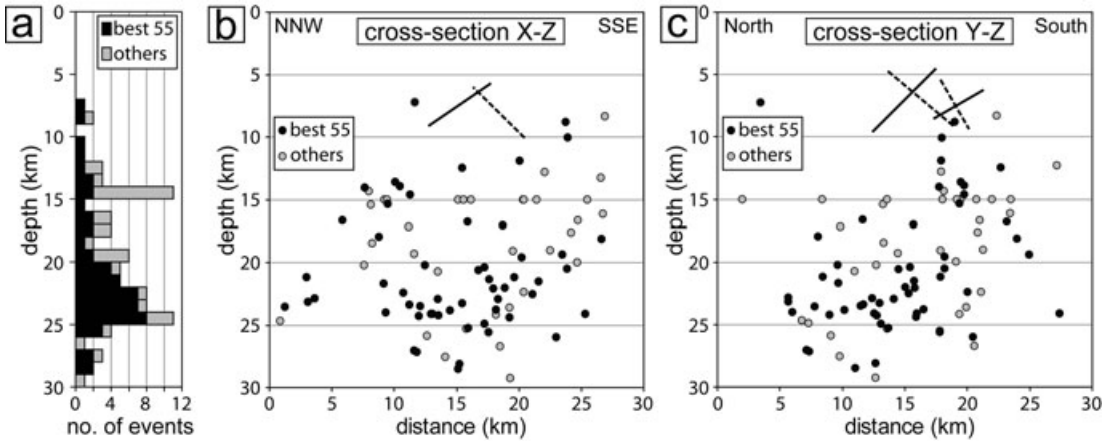

Figure 6. (a) Histogram showing hypocenter depths of locally recorded aftershocks. Black bars represent the 55 best-recorded aftershocks, with vertical errors ≤3 km, and grey bars represent a further 32 aftershocks with errors ≤5 km. (b,c) Cross-sections through the Fin region, showing projections of our model fault planes and aftershock hypocenters onto the lines *X*–*Y* and *X*–*Z* (Fig. 4). (c) Section perpendicular to the strike of faults in models A (solid line) and B (dashed line). (d) N–S section, approximately perpendicular to the strike of faults in models C (solid lines) and D (dashed lines). Black circles are the 55 best-recorded aftershocks, with vertical errors ≤3 km, and grey circles are a further 32 aftershocks with errors ≤5 km.

5 DISCUSSION

The coseismic displacements measured with InSAR arise from a single strain increment, corresponding to one part of the earthquake cycle on a single fault system. Care must therefore be taken when comparing them with the surface folding, which represents millions of years of accumulated, finite strain. Nevertheless, this comparison may still be informative, and it is one we make in this final section.

With only two components of the displacement vector (one each from ascending and descending interferograms), we were unable to measure the surface uplift directly. Instead, we computed the pattern of vertical motions predicted by our InSAR-derived earthquakes models. Fig. 4(c) shows the vertical displacements calculated for model A, with the pattern of fold axes overlain (equivalent maps for models B, C and D look very similar and are not shown here). In addition, Fig. 7(a) shows a profile through this model uplift, perpendicular to the strike of the model faults, and Fig. 7(b) shows the geology along the same transect.

Model surface uplift is centred on the common limb of the Fin syncline and the Guniz anticline, but also overlaps a section of the Fin syncline axis (Fig. 4c). The pattern of uplift is elongate in a ENE–WSW direction, oblique (by ∼20°) to the E–W trend of the surface folds. The peak uplift (>7 cm) coincides with the high parts of a distinct E–W-trending ridge, made up of N-dipping Bakhtyari conglomerates, although it is not clear whether there is a connection between the two (Fig. 4d).

The N-dipping model A fault projects to the surface at the southern edge of the Guniz anticline (Figs 5e and f and 7b). At first glance this geometry appears consistent with fault-propagation folding, with the growth of the Guniz anticline controlled by upward propagation of the N-dipping reverse fault. However, the top rupture depth (5–6 km) is small compared to the half-wavelength of the Guniz anticline (∼10 km; Fig. 7b). If growth of the Guniz anticline were controlled by this fault, one would expect it to be asymmetrical (S-verging, in the case of a N-dipping reverse fault). In reality, this anticline is strikingly concentric in shape, much more consistent with forming by buckling (Fig. 7b).

The obliquity between the pattern of surface uplift and the trend of the surface folding, the overlapping of surface uplift with part of the Fin syncline axis, and the symmetric, open nature of the local folds, all lead us to believe that locally, folding and faulting are decoupled. In the Fin region, whaleback anticlines primarily express the ∼10 km half-wavelength folding of the thick, competent Asmari limestone. The decoupling of the symmetric Fin and Guniz folds from the underlying faulting must occur stratigraphically below the Asmari limestone, suggesting a detachment within the Gurpi marls, rather than the shallower Mishan or Razak formations (Fig. 2). The space problem in the core of these detachment anticlines can be resolved by local thickening of the Gupri marls, or through the intrusion of Hormuz salt (Fig. 7b). Many of the open anticlines in this area—including Guniz—have exposures of Hormuz salt in their cores, lending further weight to this possibility (Fig. 4b).

Finally, it is worth reiterating that some other nearby anticlines, such as Ginau and Anguru (Fig. 4b, are likely to be fault-propagation folds. These strongly asymmetrical structures have steeply dipping or even overturned southern limbs, in marked contrast with the concentric, open folds in the epicentral area of the Fin earthquakes. The Simply Folded Belt therefore involves a combination of different types of folding, with forced folds above buried reverse faults, and detachment folds above weak horizons in the sedimentary cover. In this respect, our conclusions agree with structural transects across the region east of Fin by Molinaro *et al.* (2005).

6 CONCLUSIONS

The 2006 March 25 Fin earthquakes (M_w 5.7, 5.5, 5.2, 5.0, 4.9) in the south-eastern Zagros Simply Folded Belt involved buried reverse faulting within the competent, lower part of the sedimentary cover. The top depth of the rupture, at ∼5 km, was probably governed by the presence of mechanically weak Gurpi marls at this level. Locally, this horizon separates the underlying reverse faulting from the open, symmetric, surface folds, which probably formed by simple buckling of the uppermost sediments. However, some neighbouring anticlines have steepend or overturned southern limbs, consistent with growth above N-dipping faults; surface folding in the Simply Folded Belt therefore involves a combination of fault-propagation folding and detachment folding. The bottom depth of the rupture, at 9–10 km, probably corresponds with the weak, Precambrian Hormuz Salt at the base of the sedimentary cover. Locally recorded aftershocks are mostly at depths of ∼10–30 km, significantly deeper than the main rupture and probably

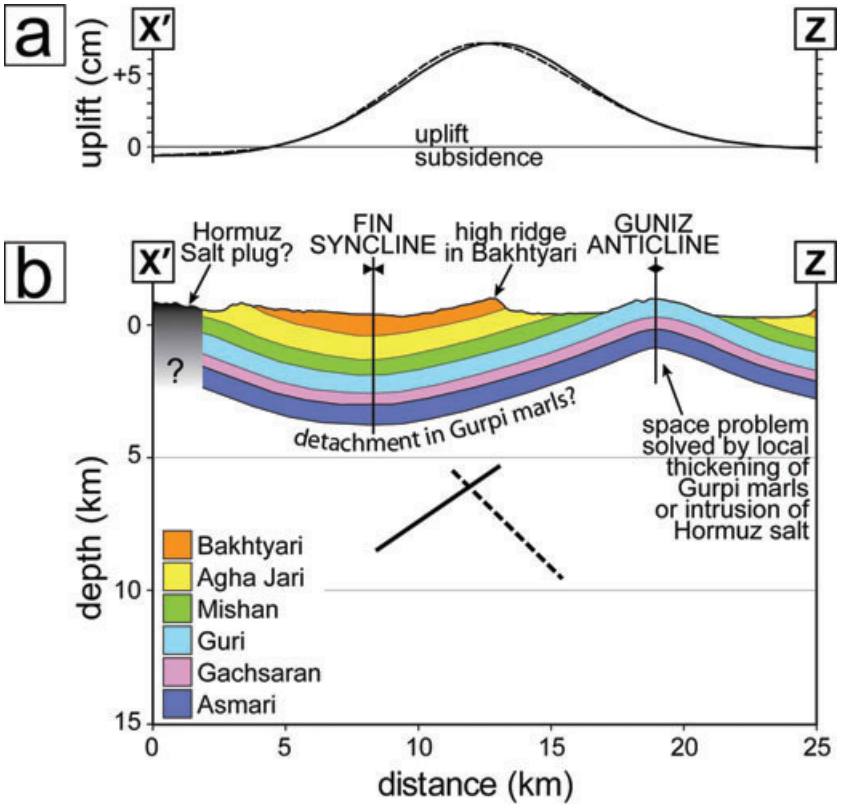

Figure 7. (a) Model surface uplift along the line *X′–Z* (Fig. 4c). Model A is shown as a solid line, and model B as a dashed line. (b) Simplified geological cross-section along the same line, constructed using a geological map of the region (National Iranian Oil Company 1999) together with SRTM topography and satellite imagery. We only include units that are directly exposed in the Fin area (Bakhtyari–Asmari), and do not try to infer the structure of the underlying Mesozoic and Paleozoic strata. The Gachsaran marls and anhydrites are the lateral equivalent of the Razak marls in Fig. 2. Model faults A and B are shown as solid and dashed lines, respectively.

within the crystalline basement. The main earthquakes therefore failed to rupture the full thickness of the seismogenic layer.

ACKNOWLEDGMENTS

This work was supported by Natural Environmental Research Council (NERC) through the National Centre for Earth Observation (NCEO), of which the Centre for the Observation and Modelling of Volcanoes, Earthquakes and Tectonics (COMET) is part. All ENVISAT ASAR data are copyrighted by the European Space Agency and were provided under project AOE-621. The authors are very grateful to Hamid Nazari and Morteza Talebian for helping to organise a short field-trip to the Fin region in 2009 April, and for discussing our work while we were there; and also to Geological Survey of Iran staff and students in Bandar Abbas and Kerman for their kind hospitality during this trip. Finally, the authors thank two anonymous reviewers for their constructive comments and suggestions.

REFERENCES

Adams, A., Brazier, R., Nyblade, A., Rodgers, A. & Al-Amri, A., 2009. Source parameters for moderate earthquakes in the Zagros Mountains with implications for the depth extent of seismicity, *Bull. seism. Soc. Am.,* **99,** 2044–2049.

Agard, P., Omrani, J., Jolivet, L. & Mouthereau, F., 2005. Convergence history across Zagros (Iran): constraints from collisional and earlier deformation, *Int. J. Earth Sci.,* **94,** 401–419.

Alavi, M., 1994. Tectonics of the zagros orogenic belt of iran: new data and interpretations, *Tectonophysics,* **229,** 211–238.

Alavi, M., 2004. Regional stratigraphy of the Zagros fold-thrust belt of Iran and its proforeland evolution, *Am. J. Sci.,* **304,** 1–20.

Alavi, M., 2007. Structures of the Zagros fold-thrust belt in Iran, *Am. J. Sci.,* **307,** 1064–1095.

Allen, M.B. & Armstrong, H.A., 2008. Arabia Eurasia collision and the forcing of mid-Cenozoic global cooling, *Palaeogeog. Palaeoclim. Palaeoecol.,* **265,** 52–58.

Allmendinger, R.W. & Shaw, J.H., 2000. Estimation of fault propagation distance from fold shape: implications for earthquake hazard assessment, *Geology,* **28,** 1099–1102.

Bahroudi, A. & Koyi, H.A., 2003. Effect of spatial distribution of Hormuz salt on deformation style in the Zagros fold and thrust belt: an analogue modelling approach, *J. geol. Soc. Lond.,* **160,** 719–733.

Baker, C., Jackson, J. & Priestley, K., 1993. Earthquakes on the Kazerun Line in the Zagros Mountains of Iran: strike-slip faulting within a fold-and-thrust belt, *Geophys. J. Int.,* **115,** 41–61.

Bayer, R. *et al.*, 2006. Active deformation in Zagros-Makran transition zone inferred from GPS measurements, *Geophys. J. Int.,* **165,** 373–381.

Berberian, M., 1995. Master blind thrust faults hidden under the Zagros folds: active basement tectonics and surface morphotectonics, *Tectonophysics,* **241,** 193–224.

Blanc, E.J.-P., Allen, M.B., Inger, S. & Hassani, H., 2003. Structural styles in the Zagros Simple Folded Zone, Iran, *J. geol. Soc. Lond.,* **160,** 401–412.

Colman-Sadd, S.P., 1978. Fold development in Zagros simply folded belt, Southwest Iran, *Am. Assoc. Petrol. Geol. Bull.,* **62,** 984–1003.

Davis, D.M. & Engelder, T., 1985. The role of salt in fold-and-thrust belts, *Tectonophysics,* **119,** 67–88.

Engdahl, E.R., van der Hilst, R.D. & Buland, R., 1998. Global teleseismic earthquake relocation from improved travel times and

procedures for depth determination, *Bull. seism. Soc. Am.,* **88,** 722–743.

Engdahl, R.E., Jackson, J.A., Myers, S.C., Bergman, E.A. & Priestley, K., 2006. Relocation and assessment of seismicity in the Iran region, *Geophys. J. Int.,* **167,** 761–778.

Falcon, N.L., 1969. Problems of the relationship between surface structure and deep displacements illustrated by the Zagros Range, in *Time and Place in Orogeny*, Special Publications No. 3, pp. 9–21, Geological Society of London, London.

Farr, T.G. & Kobrick, M., 2000. Shuttle Radar Topography Mission produces a wealth of data, *EOS, Trans. Am. geophys. Un.,* **81,** 583–585.

Gholamzadeh, A., Yamini-Fard, F., Hessami, K. & Tatar, M., 2009. The February 28, 2006 Tiab earthquake, M-w 6.0: implications for tectonics of the transition between the Zagros continental collision and the Makran subduction zone, *J. Geodyn.,* **47,** 280–287.

Hatzfeld, D., Tatar, M., Priestley, K. & Ghafory-Ashtiany, M., 2003. Seismological constraints on the crustal structure beneath the Zagros Mountain belt (Iran), *Geophys. J. Int.,* **155,** 403–410.

Hessami, K., Koyi, H.A. & Talbot, C.J., 2001a. The significance of strike-slip faulting in the basement of the Zagros fold and thrust belt, *J. Petrol. Geol.,* **24,** 5–28.

Hessami, K., Koyi, H.A., Talbot, C.J., Tabasi, H. & Shabanian, E., 2001b. Progressive unconformities within an evolving foreland fold thrust belt, Zagros Mountains, *J. geol. Soc. Lond.,* **158,** 969–981.

Jackson, J. *et al.*, 2006. Seismotectonic, rupture process, and earthquake-hazard aspects of the 2003 December 26 Bam, Iran, earthquake, *Geophys. J. Int.,* **166,** 1270–1292.

Jackson, J.A., 1980. Reactivation of basement faults and crustal shortening in orogenic belts, *Nature,* **283,** 343–346.

Jahani, S., Callot, J.-P., Letouzey, J. & Frizon de Lamotte, D., 2009. The eastern termination of the Zagros Fold-and-Thrust Belt, Iran: structures, evolution, and relationships between salt plugs, folding, and faulting, *Tectonics,* **28,** TC6004.

Jónsson, S., Zebker, H., Segall, P. & Amelung, F., 2002. fault slip distribution of the 1999 M_w 7.1 Hector Mine, California, earthquake, estimated from satellite radar and GPS measurements, *Bull. seism. Soc. Am.,* **92,** 1377–1389.

Jordan, T.H. & Sverdrup, K.A., 1981. Teleseismic location techniques and their application to earthquake clusters in the South-Central Pacific, *Bull. seism. Soc. Am.,* **71,** 1105–1130.

Kent, P.E., 1979. The emergent Hormuz salt plugs of southern Iran, *J. Petrol. Geol.,* **2,** 117–144.

Kissling, E., 1988. Geotomography with local earthquake data, *Rev. Geophys.,* **26,** 659–698.

Lee, W.H.K. & Lahr, J.C., 1972. HYPO71 (revised), a computer program for determining hypocenters, magnitude and first motion pattern of local earthquakes, U.S. Geological Survey Open File Report, pp. 75–311.

Lohman, R.B. & Simons, M., 2005. Locations of selected small earthquakes in the Zagros mountains, *Geochem. Geophys. Geosyst.,* **6,** Q03001.

McCaffrey, R. & Abers, G., 1988. SYN3: A Program for Inversion of Teleseismic Body Wave Forms on Microcomputers, Air Force Geophysical Laboratory Technical Report, Hanscomb Air Force Base, Massachusetts.

McQuarrie, N., 2004. Crustal scale geometry of the Zagros fold-thrust belt, Iran, *J. Struct. Geol.,* **26,** 519–535.

McQuarrie, N., Stock, J.M., Verdel, C. & Wernicke, B.P., 2003. Cenozoic evolution of Neotethys and implications for the causes of plate motions, *Geophys. Res. Lett.,* **30**(20), 2036.

Mitra, S., 2003. A unified kinematic model for the evolution of detachment folds, *J. Struct. Geol.,* **25,** 1659–1673.

Molinaro, M., Guezou, J.-C., Leturmy, P., Eshraghi, S.A. & Frizon de Lamotte, D., 2004. The origin of changes in structural style across the Bandar Abbas syntaxis, SE Zagros (Iran), *Marine. Petrol. Geol.,* **21,** 735–752.

Molinaro, M., Leturmy, P., Guezou, J.-C., Frizon de Lamotte, D. & Eshraghi, S.A., 2005. The structure and kinematics of the southeastern Zagros fold-thrust belt, Iran: from thin-skinned to thick-skinned tectonics, *Tectonics,* **24,** TC3007.

Molnar, P. & Lyon-Caen, H., 1989. Fault plane solutions of earthquakes and active tectonics of the Tibetan Plateau and its margins, *Geophys. J. Int.,* **99,** 123–154.

Mouthereau, F., Tensi, J., Bellahsen, N., Lacombe, O., De Boisgrollier, T. & Kargar, S., 2007. Tertiary sequence of deformation in a thin-skinned/thick-skinned collision belt: the Zagros Folded Belt (Fars, Iran), *Tectonics,* **26,** TC5006.

National Iranian Oil Company, 1999. Geological map of Iran quadrangle, I-13, Bandar Abbas, 1/250,000, Tehran.

Ni, J. & Barazangi, M., 1986. Seismotectonics of the Zagros continental collision zone and a comparison with the Himalayas, *J. geophys. Res.,* **91**(B8).

Nissen, E., Ghorashi, M., Jackson, J., Parsons, P. & Talebian, M., 2007. The 2005 Qeshm Island earthquake (Iran) – a link between buried reverse faulting and surface folding in the Zagros Simply Folded Belt?, *Geophys. J. Int.,* **171,** 326–338.

O' Brien, C.A.E., 1957. Salt diapirism in south Persia, *Geologie en Mijnbouw,* **19,** 357–376.

Okada, Y., 1985. Surface deformation due to shear and tensile faults in a half-space, *Bull. seism. Soc. Am.,* **75,** 1135–1154.

Oveisi, B., Lavé, J., van der Beek, P., Carcaillet, J., Benedetti, L. & Aubourg, C., 2009. Thick- and thin-skinned deformation rates in the central Zagros simple folded zone (Iran) indicated by displacement of geomorphic surfaces, *Geophys. J. Int.,* **176,** 627–654.

Parsons, B. *et al.*, 2006. The 1994 Sefidabeh (eastern Iran) earthquakes revisited: new evidence from satellite radar interferometry and carbonate dating about the growth of an active fold above a blind thrust fault, *Geophys. J. Int.,* **164,** 202–217.

Peyret, M., Rolandone, F., Dominguez, S., Djamour, Y. & Meyer, B., 2008. Source model for the Mw 6.1, 31 March 2006, Chalan-Chulan Earthquake (Iran) from InSAR, *Terra Nova,* **20,** 126–133.

Press, W.H., Teukolsky, S.A., Vetterling, W.T. & Flannery, B.P., 1992. *Numerical Recipes in C: The Art of Scientific Computing*, Cambridge University Press, Cambridge.

Regard, V., Bellier, O., Thomas, J., Abbassi, M.R., Mercier, J., Shabanian, E., Feghhi, K. & Soleymani, S., 2004. Accommodation of Arabia-Eurasia convergence in the Zagros-Makran transfer zone, SE Iran: a transition between collision and subduction through a young deforming system, *Tectonics,* **23,** TC4007.

Scholz, C.H., 1982. Scaling laws for large earthquakes: consequences for physical models, *Bull. seism. Soc. Am.,* **72,** 1–14.

Semmane, F., Cotton, F. & Campillo, M., 2005. The 2000 Tottori earthquake: a shallow earthquake with no surface rupture and slip properties controlled by depth, *J. geophys. Res.,* **110**(B9), 03306.

Sepehr, M., Cosgrove, J. & Moieni, M., 2006. The impact of cover rock rheology on the style of folding in the Zagros fold-thrust belt, *Tectonophysics,* **427,** 265–281.

Sherkati, S. & Letouzey, J., 2004. Variation of structural style and basin evolution in the central Zagros (Izeh zone and Dezful Embayment), Iran, *Marine. Petrol. Geol.,* **21,** 535–554.

Sherkati, S., Molinaro, M., Frizon de Lamotte, D. & Letouzey, J., 2005. Detachment folding in the Central and Eastern Zagros fold-belt (Iran): salt mobility, multiple detachments and late basement control, *J. Struct. Geol.,* **27,** 1680–1696.

Sherkati, S., Letouzey, J. & Frizon de Lamotte, D., 2006. Central Zagros fold-thrust belt (Iran): New insights from seismic data, field observation, and sandbox modeling, *Tectonics,* **25,** TC4007.

Stein, R.S. & King, G.C.P., 1984. Seismic potential revealed by surface folding: 1983 Coalinga, California, Earthquake, *Science,* **224,** 869–872.

Stöcklin, J., 1968. Structural history and tectonics of iran: a review, *Am. Assoc. Petrol. Geol. Bull.,* **52,** 1229–1258.

Suppe, J., 1983. Geometry and kinematics of fault-bend folding, *Am. J. Sci.,* **283,** 684–721.

Suppe, J. & Medwedeff, D.A., 1990. Geometry and kinematics of fault-propogation folding, *Eclogae Geol. Helvetiae,* **83,** 409–454.

Suppe, J. & Namson, J., 1979. Fault-bend origin of frontal folds of the western Taiwan fold-and-thrust belt, *Petrol. Geol. Taiwan,* **16,** 1–18.

Talebian, M. & Jackson, J., 2002. Offset on the Main Recent Fault of NW Iran and implications for the late Cenozoic tectonics of the Arabia-Eurasia collision zone, *Geophys. J. Int.,* **150,** 422–439.

Talebian, M. & Jackson, J., 2004. A reappraisal of earthquake focal mechanisms and active shortening in the Zagros mountains of Iran, *Geophys. J. Int.,* **156,** 506–526.

Tatar, M., Hatzfeld, D. & Ghafory-Ashtiany, M., 2004. Tectonics of the Central Zagros (Iran) deduced from microearthquake seismicity, *Geophys. J. Int.,* **156,** 255–266.

Tatar, M., Hatzfeld, D., Moradi, A.S. & Paul, A., 2005. The 2003 December 26 Bam earthquake (Iran), Mw 6.6, aftershock sequence, *Geophys. J. Int.,* **163,** 90–105.

Vernant, P. *et al.*, 2004. Present-day crustal deformation and plate kinematics in the Middle East constrained by GPS measurements in Iran and northern Oman, *Geophys. J. Int.,* **157,** 381–398.

Walker, R.T., Andalibi, M.J., Gheitanchi, M.R., Jackson, J.A., Karegar, S. & Priestley, K., 2005. Seismological and field observations from the 1990 November 6 Furg (Hormozgan) earthquake: a rare case of surface rupture in the Zagros mountains of Iran, *Geophys. J. Int.,* **163,** 567–579.

Walpersdorf, A. *et al.*, 2006. Difference in the GPS deformation pattern of North and Central Zagros (Iran), *Geophys. J. Int.,* **167,** 1077–1088.

Werner, C., Wegmüller, U., Strozzi, T. & Wiesmann, A., 2000. GAMMA SAR and interferometric processing software, ERS–Envisat Symposium, Gothenburg, Sweden.

Wright, T.J., Parsons, B.E., Jackson, J.A., Haynes, M., Fielding, E.J., England, P.C. & Clarke, P.J., 1999. Source parameters of the 1 October 1995 Dinar (Turkey) earthquake from SAR interferometry and seismic body-wave modelling, *Earth planet. Sci. Lett.,* **172,** 23–37.

Wright, T.J., Lu, Z. & Wicks, C., 2004. Constraining the slip distribution and fault geometry of the M-w 7.9, 3 November 2002, Denali fault earthquake with interferometric synthetic aperture radar and global positioning system data, *Bull. seism. Soc. Am.,* **94,** 175–189.

Yamini-Fard, F., Hatzfeld, D., Farahbod, A.M., Paul, A. & Mokhtari, M., 2007. The diffuse transition between the Zagros continental collision and the Makran oceanic subduction (Iran): microearthquake seismicity and crustal structure, *Geophys. J. Int.,* **170,** 182–194.

Yielding, G., Jackson, J.A., King, G.C.P., Sinvhal, H., Vita-Finzi, C. & Wood, R.M., 1981. Relations between surface deformation, fault geometry, seismicity, and rupture characteristics during the El Asnam (Algeria) earthquake of 10 October 1980, *Earth planet. Sci. Lett.,* **56,** 287–304.

Zwick, P., McCaffrey, R. & Abers, G., 1994. MT5 Program, *IASPEI Software Library,* **4**.

APPENDIX A: *P*- AND *SH*-BODYWAVE MODELS

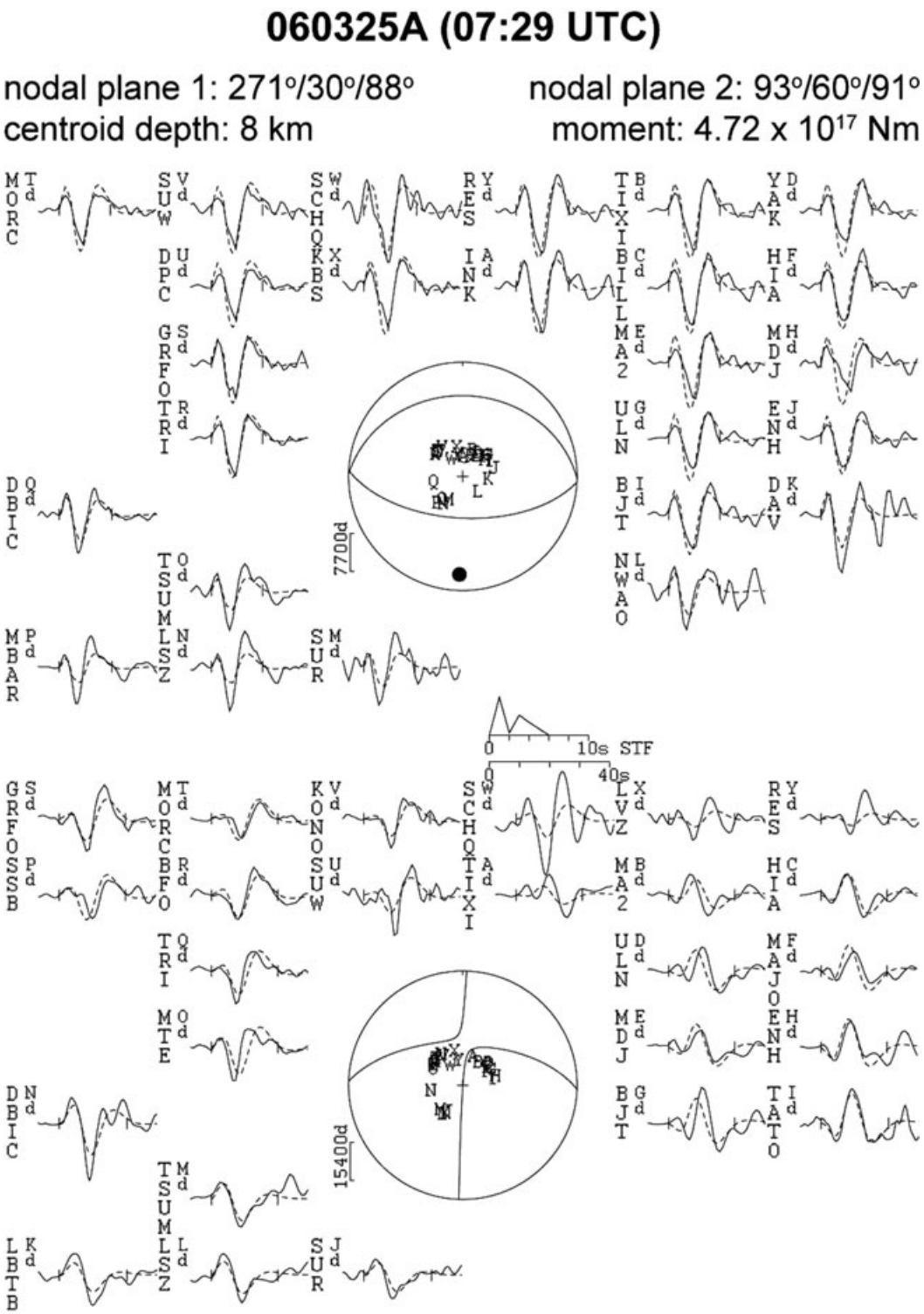

Figure A1. Minimum misfit solution for the first 2006 March 25 earthquake (07:29 UTC), calculated by inverting *P* and *SH* bodywaves for a point source in a half space of $V_p = 5.7$ m s^{-1}, $V_s = 3.3$ m s^{-1} and $\rho = 2.6 \times 10^3$ kg m^{-3} (consistent with the uppermost layer in the velocity structure calculated from locally recorded aftershock arrival times). The focal spheres show *P*- (top) and *SH*- (bottom) nodal planes in lower hemisphere projections; closed and open circles represent the *P*- and *T*-axes, respectively. Observed (solid) and synthetic (dashed) waveforms are plotted around the focal spheres; the inversion window is indicated by vertical ticks, station codes are written vertically and station positions denoted by capital letters. The STF is the source time function, and the scale bar below it (in seconds) is that of the waveforms.

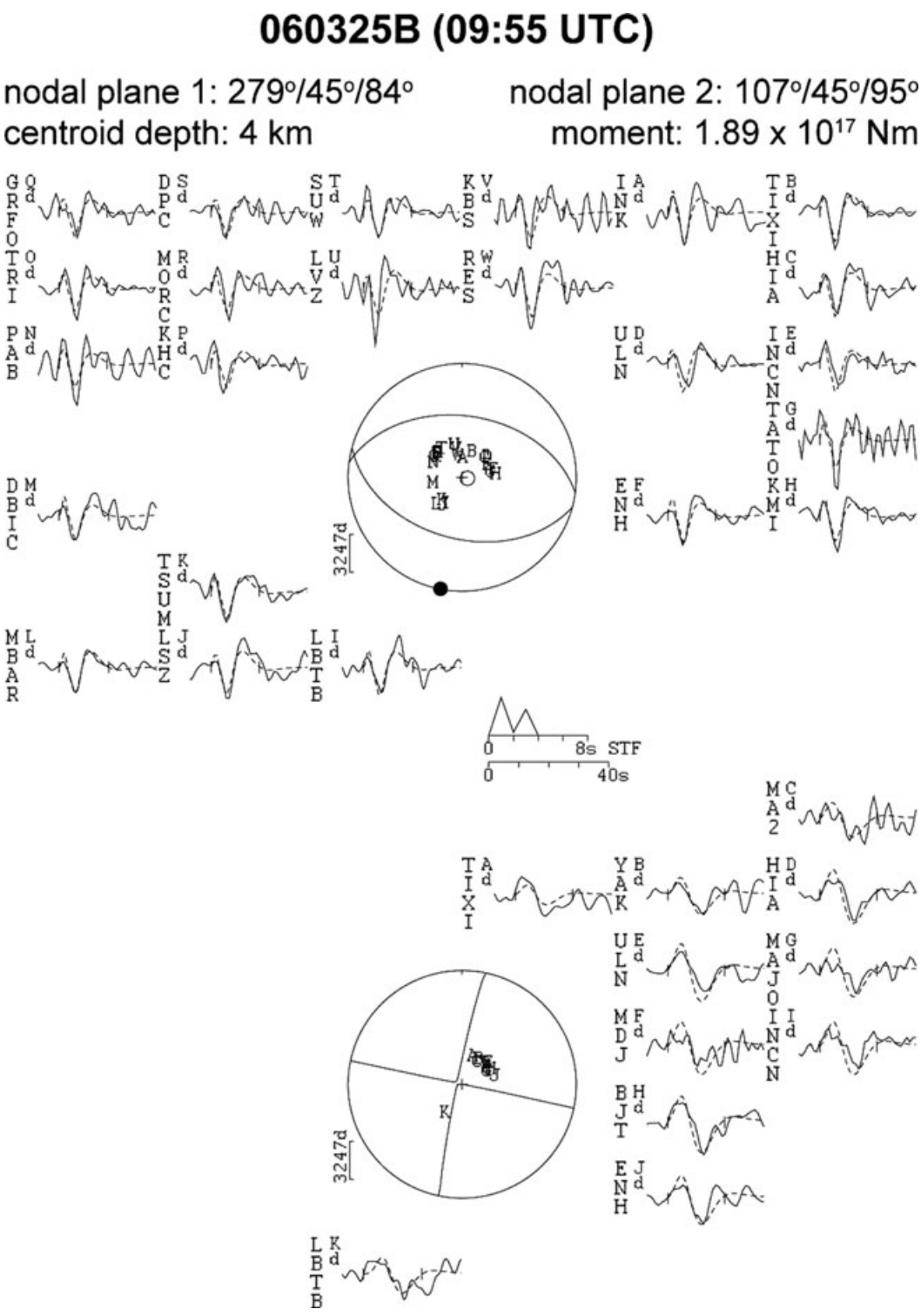

Figure A2. Minimum misfit solution for the second 2006 March 25 earthquake (09:55 UTC) from *P*- and *SH*-bodywave modelling. The layout is the same as for Fig. A1.

APPENDIX B: EARTHQUAKE SCALING RELATIONS

To estimate the fault plane dimensions and fault slip of the 07:29 and 09:55 earthquakes, we use the relationship

$$M_o = \mu A \bar{u},$$

where M_o is the moment; μ is the shear modulus (we use a value of 2.8×10^{10} Pa, consistent with the velocity of the uppermost layer calculated in the Section 4); A is the fault plane area and $\bar{u}$ is the fault slip.

After Scholz (1982), we also use the empirical relationship

$$\bar{u}/L \approx 5 \times 10^{-5},$$

where L is the fault length. Considering the moderate size of the earthquakes, we also assume that the length of the fault plane in each earthquake is equal to its width, such that $A = L^2$.

From these relations,

$$L = \sqrt[3]{M_o/(\mu \times 5 \times 10^{-5})}$$

and

$$\bar{u} = \sqrt[3]{(M_o \times 2.5 \times 10^{-9})/\mu}$$

APPENDIX C: LOCALLY RECORDED AFTERSHOCKS

Table C1. Our preferred velocity structure, determined by inverting the arrival-times of the 87 best-recorded aftershocks.

Layer	V_p (km s^{-1})	Depth of top (km)
1	5.65	0
2	5.90	12
Half-space	6.25	18

Table C2. Fifty-five selected, locally recorded aftershocks.

Date	Time	Latitude	Longitude	Depth (km)	Mag	No.	Gap	Dmin (km)	RMS	Ez (km)	Eh (km)	S-P	P
March 26	03:22:43.04	27.70083	55.93317	7.24	2	4	176	3.3	0.00	0.0	0.0	1	1
April 12	17:31:50.87	27.66683	55.83533	27.07	1	11	140	8.3	0.13	1.3	1.1	6	2
April 12	22:42:04.52	27.59367	55.88967	22.52	2	8	178	13.2	0.12	2.1	2.1	5	2
April 13	00:46:24.18	27.63183	55.83317	28.52	2	11	152	11.2	0.17	1.8	1.7	6	2
April 13	01:04:49.78	27.66517	55.83650	27.15	1	8	140	8.3	0.07	0.9	0.8	6	2
April 13	01:28:09.05	27.58750	55.82050	24.42	3	11	168	16.0	0.23	2.1	2.7	5	2
April 13	02:17:13.78	27.61333	55.83916	24.94	2	12	157	12.6	0.25	2.1	2.3	6	2
April 13	02:26:39.67	27.63950	55.83767	23.82	1	8	172	25.7	0.09	1.7	1.6	4	1
April 13	02:29:01.37	27.51467	55.81717	18.14	2	9	193	25.8	0.21	3.0	3.3	4	1
April 13	02:43:41.40	27.65050	55.84300	24.24	1	12	144	9.0	0.14	1.3	1.2	6	2
April 13	02:54:30.57	27.60400	55.84200	22.94	1	8	160	13.4	0.16	1.7	2.3	4	2
April 13	02:56:41.87	27.56767	55.89117	20.49	3	15	165	16.0	0.22	1.3	1.7	6	2
April 13	05:53:08.59	27.58950	55.89150	21.50	2	12	158	13.6	0.24	1.8	2.3	6	2
April 13	11:10:48.69	27.54633	55.80767	25.99	1	5	184	28.6	0.02	0.9	0.5	2	1
April 13	15:02:28.39	27.56017	55.86817	8.84	1	8	171	6.4	0.13	1.1	1.7	6	3
April 14	20:41:24.81	27.64300	55.70033	21.70	1	10	164	14.6	0.18	1.9	1.7	8	3
April 15	04:52:23.45	27.67833	55.63417	23.19	2	9	173	7.6	0.14	1.8	1.3	7	3
April 16	12:27:52.22	27.56983	55.89933	10.07	1	8	163	3.2	0.23	2.1	1.7	5	3
April 16	18:28:24.67	27.64400	55.79500	20.25	2	11	152	13.0	0.11	1.0	0.9	7	3
April 16	22:42:40.60	27.67833	55.64817	22.86	1	10	173	9.0	0.12	1.4	1.1	8	3
April 17	02:20:21.86	27.65750	55.73117	17.99	2	8	153	17.3	0.25	2.8	2.1	6	3
April 17	13:27:30.69	27.56983	55.72450	25.60	1	12	191	20.3	0.15	1.9	1.6	8	3
April 18	00:51:55.45	27.62683	55.73600	23.53	1	11	166	18.5	0.15	1.5	1.4	8	3
April 18	04:08:07.44	27.59567	55.83417	22.02	2	6	181	10.1	0.10	1.6	1.6	6	3
April 19	03:36:31.26	27.61483	55.69850	24.29	1	10	126	15.6	0.10	1.2	1.4	8	4
April 19	19:01:43.21	27.67683	55.80067	24.01	1	8	159	10.7	0.22	2.7	2.2	7	3
April 19	19:20:20.05	27.58883	55.78067	21.36	3	11	174	15.1	0.14	1.4	1.5	8	3
April 19	19:33:47.65	27.60000	55.78733	20.60	2	8	169	14.7	0.20	2.1	2.3	6	3
April 19	22:11:41.61	27.65283	55.55867	21.17	2	7	137	2.6	0.16	2.4	1.6	7	3
April 20	04:41:57.29	27.60717	55.78650	25.28	2	7	182	15.0	0.06	1.0	0.8	8	3
April 20	10:06:09.94	27.58533	55.64483	24.10	2	10	133	13.3	0.10	1.1	1.5	8	4
April 20	15:09:11.41	27.62400	55.55684	16.65	2	6	135	5.8	0.06	0.9	1.0	6	3
April 20	18:20:36.30	27.61733	55.73183	24.12	2	12	127	18.5	0.19	1.6	1.8	9	4
April 21	22:36:20.37	27.62450	55.70517	23.40	1	5	186	15.7	0.00	0.1	0.1	5	3
April 22	03:22:55.61	27.52383	55.53633	12.46	3	19	151	13.3	0.22	1.3	1.9	9	4
April 22	05:28:36.05	27.55000	55.49567	14.65	3	5	150	10.9	0.04	1.1	1.3	4	2
April 22	22:57:39.58	27.54717	55.47333	22.43	3	9	163	9.0	0.24	2.5	2.2	9	4
April 22	22:59:43.79	27.51933	55.53567	16.80	2	6	174	13.1	0.08	1.5	2.2	6	4
April 23	02:10:16.44	27.65817	55.52650	23.55	1	9	203	3.6	0.20	2.1	1.6	8	4
April 28	00:52:46.10	27.56983	55.78150	21.17	3	14	181	14.9	0.14	1.3	1.2	8	3
April 28	00:54:18.47	27.58833	55.78700	22.07	2	8	173	14.5	0.09	1.2	1.2	7	3
April 28	01:24:52.44	27.56700	55.79033	19.58	1	14	180	14.0	0.14	1.1	1.1	7	3
April 28	15:23:29.11	27.61400	55.79167	23.30	2	10	163	14.8	0.19	2.0	1.9	7	3
April 28	16:02:34.08	27.59183	55.77800	20.38	2	9	173	15.4	0.28	2.7	2.9	7	3
April 29	02:05:02.94	27.61883	55.75467	22.91	2	10	126	17.8	0.15	1.7	2.2	8	4
April 30	17:49:12.14	27.61683	55.79433	28.13	3	7	180	24.3	0.09	1.9	0.9	4	1
March 06	04:16:49.18	27.55300	55.45517	15.36	3	20	182	8.3	0.20	1.3	0.9	8	3
March 06	06:39:16.53	27.54967	55.47300	13.93	1	11	165	9.2	0.13	1.0	1.0	8	3
March 06	22:36:25.74	27.56733	55.44584	14.04	1	9	198	9.3	0.09	0.9	0.9	8	3
March 07	23:53:16.91	27.50483	55.70350	19.39	2	14	178	23.9	0.17	1.1	2.4	8	3
March 08	09:49:40.33	27.55183	55.46917	13.63	1	7	170	9.1	0.13	1.9	2.7	7	3
March 09	01:38:56.42	27.58967	55.81217	17.05	1	9	188	16.2	0.17	1.6	1.4	6	2
March 10	13:51:11.87	27.48283	55.69200	24.14	2	10	170	25.3	0.07	0.9	1.9	6	3
March 12	08:47:03.47	27.56917	55.79200	11.91	2	13	139	19.2	0.29	1.4	2.1	4	2
March 12	21:09:55.72	27.58200	55.77600	23.81	1	12	136	19.0	0.20	1.5	2.4	8	3

Note: *No.* is the total number of *P* and *S* phases recorded for each event; *Gap* is the largest azimuthal gap between stations (in degrees); *Dmin* is the minimum station distance from the epicentre; *Ez* and *Eh* are vertical and horizontal errors in the hypocenter locations; *RMS* is the root mean square of the residual time between the observed and calculated arrival times of *P* and *S* waves (in seconds). *S–P* is the total number of *P* and *S* phases recorded at the closest five stations, and *P* is the number of *P* arrivals recorded at the closest four stations.